Applied Water Science (2024) 14:131
https://doi.org/10.1007/s13201-024-02197-0

ORIGINAL ARTICLE

An in-depth analysis of the hydrodynamic behaviour of a high-rate lamellar DAF tank by means of CFD simulations

Dmytro Hlukhov[1] · Gorka S. Larraona[1] · Alejandro Rivas[1] · Juan Carlos Ramos[1]

Received: 20 July 2023 / Accepted: 16 April 2024

Abstract

This research is based on computational fluid dynamics simulations of water and microbubble flow within the tank of a lamellar DAF (L-DAF) clarification system operating under high-rate DAF conditions (12–30 m/h). Firstly, performance of the DAF tank with lamellae was evaluated under two operating conditions in which the flow was either short-circuited or stratified in the absence of lamellae. In addition, the improvement in bubble removal efficiency achieved by the incorporation of lamellae in each scenario was assessed. Secondly, an in-depth analysis was conducted of the flow that develops in the separation zone as a result of placing the lamella pack in that part of the tank. The significant density difference that the lamellae cause to exist between the bubble blanket and clarified water below is responsible for the complex three-dimensional flow observed between the two regions. Analysis of this flow showed a previously undescribed mechanism in which the density gradient plays a crucial role in preventing bubbles from passing through the lamellae and ultimately escaping with the effluent. Finally, the effect of hydraulic loading on the bubble removal efficiency of the L-DAF tank under consideration was researched, and it was found that an L-DAF with a height/length ratio of 0.72 is able to operate at hydraulic loading close to 30 m/h, evidencing good debubbling performance.

Keywords Dissolved Air Flotation · Lamellae · Lamellar DAF · High-rate DAF · Computational Fluid Dynamics · Removal efficiency

Introduction

Dissolved air flotation (DAF) is a treatment method widely used in the field of drinking water clarification and sludge thickening (Haarhoff and van Vuuren 1995). A recent study showed that DAF can be an excellent complementary method to remove total suspended solids (TSS), and chemical oxygen demand when employed after a high-rate sludge activation system has been applied (Cagnetta et al. 2019). Soares et al. (2021) demonstrate that it is possible to use DAF in the diagnosis of intestinal parasites in faeces in municipal waters and that this may be a promising new research route. Piaggio et al. (2022) argue that DAF can be especially efficient in removing TSS when placed downstream from an anaerobic bioreactor or adjacent to the source of contamination, with solid removal exceeding 90%.

The flotation tanks in DAF systems consist of a contact zone (CZ) and a separation zone (SZ), which are divided by a baffle. The separation between suspended solids (SS) and water is achieved by flotation after introducing microscopic air bubbles in the recycle-flow and establishing favourable conditions for these to attach to the surface of the material to be removed. As a result of collisions in the CZ, clusters of multiple particles and air bubbles, also called aggregates, are formed, whose density is lower than that of the surrounding liquid. The higher floating velocity of these aggregates allows them to rise to the free surface of the SZ, where they are subsequently removed by mechanical means (Edzwald 2010a).

The flow structure inside DAF tanks is mainly governed by hydraulic loading (total flow rate divided by the plan area of the SZ) and the amount of air injected and was characterised by (Lundh et al. 2000, 2001; Lundh 2002; Lundh and Jönsson 2005) for a broad range of both parameters. On the one hand, when the air content is high enough, a stratified

✉ Gorka S. Larraona
gsanchez@tecnun.es

[1] Departamento de Ingeniería Mecánica y Materiales, Universidad de Navarra, TECNUN Escuela de Ingeniería, Manuel de Lardizábal 13, 20018 San Sebastián, Spain

Published online: 13 May 2024

flow structure is produced. This structure is characterised by the difference in density between the current entering the SZ from the CZ and the water already in the tank. Its lower density causes the current to move horizontally from the baffle to the far end wall and may even return in a layer immediately below, thus forming a stable bubble blanket that favours the removal of SS. On the other hand, when the air content is insufficient, a phenomenon known as short-circuit or break-through frequently occurs, in which the current entering the SZ flows through the bubble blanket and creates a preferential path to the outlet, allowing SS and bubbles to escape through the latter.

The prevailing trend in water treatment plants to maximise the treated flow rate has resulted in the need for the design of DAF systems that run at higher hydraulic loadings (HL) than the 5–15 m/h of conventional DAF, reaching values up to 15–30 m/h (or even 40 m/h) in what are known as high-rate DAF (Edzwald 2010b). Raising the air content by increasing the air saturation pressure and/or the recycle-flow rate is one way to attain such a high HL and prevent the development of short-circuit; however, this is an energy-intensive solution. Another possibility is the employment of a DAF tank with a square bottom, significant height (i.e. a high height/length ratio), and a perforated plate at the bottom (Kiuri 2001). Alternatively, using lamella packs (Reali and Marchetto 2001; Echeverri and Rein 2007; Jokela and Lepistö 2014) or a combination of these with a perforated plate (Hedberg et al. 1998; Fang et al. 2009; Azevedo et al. 2018) has been proposed, and numerous companies currently manufacture DAF systems with these components (Crossley and Valade 2006). The lamella packs are placed in the SZ and are similar to those used in settlers, i.e. a collection of inclined tubes or flat plates, but operate in the opposite way. The clarified water escapes from the bottom of the lamellae, whereas flotation retains bubbles and agglomerates at the upper part of the lamella pack.

Comparatively, there has been less scientific research on DAF tanks with lamella elements than on lamellar settling tanks, and practically all of these studies have focused on the flat-plate lamella type. Published research demonstrates conclusively that the addition of lamellae greatly improves the HL at which the DAF system can operate while maintaining appropriate efficiency. Haarhoff and Vuuren (1993) describe some of the earliest applications that integrated lamellae and claims that a doubling of the HL was achieved. Hedberg et al. (1998) and Amato et al. (2001) conducted thorough research using pilot plants with various flat-plate lamella packs and achieved hydraulic loadings between 20 and 40 m/h (or even higher) while preserving clarified water turbidity below 1 NTU. Fang et al. (2009) achieved 95% turbidity removal at 18 m/h by combining flat plate lamellae with an underlying perforated plate. Jokela and Lepistö (2014) employed U-shaped lamellae and achieved HL up to 21 m/h with very significant removal of phosphorus and nitrogen from the effluent of a fish farm. Azevedo et al. (2018) designed a flat-plate lamellar DAF tank with HL of 15 m/h that efficiently removed metal ions and tiny solid particles from mine wastewater.

The description of the flow in DAF tanks with lamellae (L-DAF) has been mainly based on visualisation through windows or transparent sidewalls in the pilot plants. Hedberg et al. (1998) and Fang et al. (2009) noticed that the depth of the bubble blanket decreased when there were lamellae, but the blanket was more compact, and its border with the clarified water below was clearly discernible. Nonetheless, when HL increased, the bubble blanket became deeper (Fang et al. 2009). Hedberg et al. (1998) assessed whether when HL increased, the rising velocity of the bubbles between the lamellae slowed due to the increased drag of the incoming water flow. When HL was too high, Jokela and Lepistö (2014) found that the flocs were carried away by this downward flow of water. Using coloured ink, Moruzzi and Reali (2014) observed that the water flow was more uniformly distributed across the lamellae when the clarified water was evacuated through a perforated plate beneath the lamellae. On the other hand, most authors (Hedberg et al. 1998; Fang et al. 2009; Moruzzi and Reali 2014; Azevedo et al. 2018) emphasised the fact that by placing lamellae in the SZ, three-dimensional flow structures that could destabilise the bubble blanket were avoided, and laminar flow conditions were achieved. This phenomenon was attributed by Hedberg et al. (1998) to the substantial density gradient between the compact bubble blanket and the clarified water, which prevented the turbulence of the former from penetrating the latter.

Although the beneficial effects of using lamella elements in DAF tanks have been thoroughly detailed, the mechanism by which lamellae prevent the bubbles (and aggregates) carried between them by the water current from reaching the outlet has not been examined in depth. Based on the flow visualisation they performed in a pilot plant with a transparent sidewall, Hedberg et al. (1998) described this mechanism as the opposite of that which takes place in counter-current lamellar settlers. According to the authors, as the water current flows downwards between the lamellae, the bubbles float and attach to the lamella plates from under, where they create larger bubbles that exit the top of the lamella pack when they have sufficient lift to overcome the downward current. Subsequently, Jokela and Lepistö (2014) pointed out that they observed an aggregate behaviour comparable to that described by Hedberg et al. (1998) in their U-shaped lamellae. In addition, Echeverri and Rein (2007) referred to the same mechanism in their computational study of a circular syrup clarifier and verified the fact that aggregates that get between the lamellae ascend towards the bottom side of the latter, with higher rising velocity the greater their size. Nowadays, catalogues of industrial L-DAF systems refer to

this mechanism as the one describing the functioning of lamella packs.

The use of experimental methods to analyse the functioning of lamellae in DAF tanks is very complicated beyond the simple visualisation that can be done through transparent walls. In this context, CFD (computational fluid dynamics) simulations are offered as a powerful alternative tool for the purpose of conducting this analysis. Numerous publications have used CFD simulations to analyse the flow in DAF tanks without lamellae in industrial (Kwon et al. 2006; Emmanouil et al. 2007; Amato and Wicks 2009; Satpathy et al. 2020) and pilot size tanks (Bondelind et al. 2010b; Lakghomi et al. 2015; Hlukhov et al. 2022). In a recent study, Hlukhov et al. (2022) examined the conditions under which stratification occurred in the SZ of Lundh's pilot tank (Lundh et al. 2001), with the authors introducing and proving that the critical bubble diameter concept is a valuable tool in CFD analyses of DAF tanks. However, to the best knowledge of the authors, there has been no CFD study of a DAF tank with lamellae in water clarification applications.

The presence of lamellae has a significantly positive effect on the performance of DAF. However, scientific evidence is insufficient to explain the phenomena occurring within the lamella pack and their effect on the hydraulic behaviour of the separation zone. In this research, the multiphase hydrodynamics of a DAF tank with integrated lamellae will be covered in detail, and comparison and analysis of the flow patterns of a DAF with and without lamella pack conducted. The three-dimensional behaviour of the water flow outside and within the lamella pack, as well as the favourable hydraulic conditions offered by the lamellae, will also be described. A novel mechanism for explaining the operation of lamellae will be proposed and discussed, and finally, the air removal performance of a DAF tank in the presence and absence of lamellae under a variety of hydraulic loadings ranging from conventional to high-rate values will be studied.

Materials and methods

The research work was conducted by adding a flat-plate lamella pack to a computational model of the DAF tank employed in the experimental studies carried out by Lundh et al. (2000, 2001, 2002). Only water and microbubbles were considered in the simulations, in accordance with the approach of taken by these authors and the vast majority of previously conducted CFD research in DAF tanks without lamellae (Amato and Wicks 2009; Bondelind et al. 2010b; Emmanouil et al. 2011; Lakghomi et al. 2012; Hlukhov et al. 2022). In the case of low SS concentrations, Lundh et al. (2001) demonstrated that the presence of flocs had no major effect on the flow structure. This approach was also considered to be appropriate for the purpose of analysing the flow within a DAF tank with lamella elements, as well as to evaluate the performance of the tank under various operating conditions, using the bubble removal efficiency as a first approximation of SS removal efficiency (Lakghomi et al. 2012).

The tank's main dimensions are $1.24 \times 1.71 \times 0.$ m^3 (height/length ratio of 0.72), and it features a baffle with a height of 87 cm dividing the CZ and the SZ, as well as three injection pipes for the recycled-flow and a collection system for the clarified water via two pipes with perforated bottoms (Fig. 1b). The tank but without lamellae was analysed by simulation by the present authors, and the same physical models and boundary conditions were employed in this work. To the previously validated CFD model of this tank,

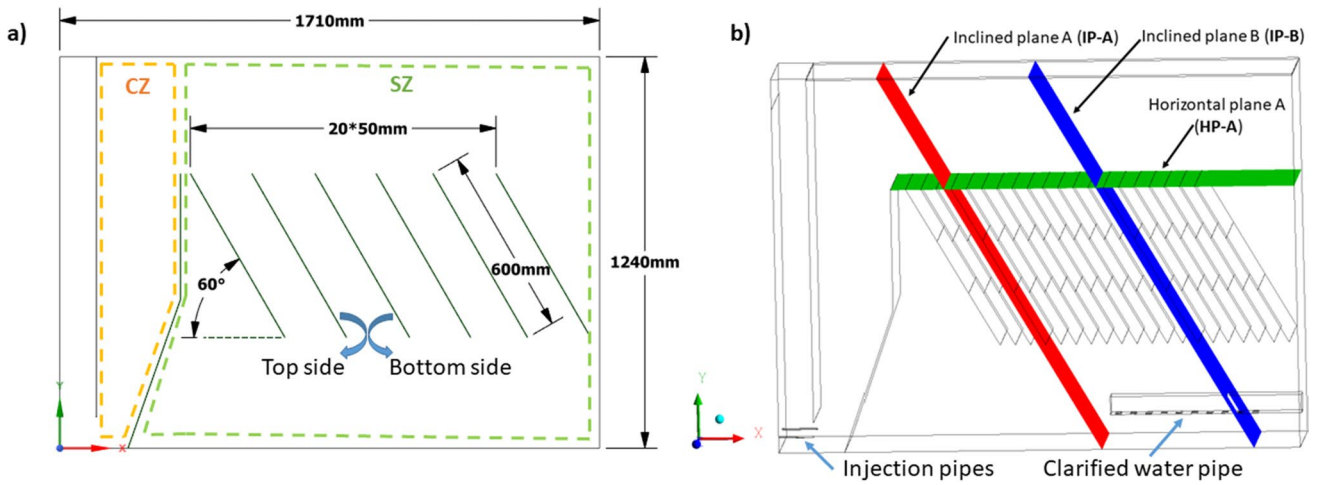

Fig. 1 Simplified schematic of L-DAF with the most pertinent dimensions (**a**) and geometry of the computational model and position of the inclined planes IP-A and IP-B as well as the horizontal plane HP-A (**b**)

20 flat lamellae without thickness were added to the separation zone, with the upper edge of the lamella pack placed at the height of the baffle edge (see Figs. 1a and 2). As in Hedberg et al. (1998), the lamellae were 60 cm in length, and the 5-cm spacing between the plates is comparable to that utilised by other authors (Hedberg et al. 1998; Echeverri and Rein 2007; Fang et al. 2009). As indicated in Fig. 1a, the two sides of the lamella were designated as "top side" and "bottom side."

It was decided to position the lamellae at a 60-degree angle to the horizontal plane (see Fig. 1a). Hedberg et al. (1998) evaluated different lamella inclinations and advised against using angles of less than 40 degrees, since this would substantially diminish the velocity at which accumulated bubbles on the bottom side of the lamellae ascend. Echeverri and Rein (2007) also used a 60-degree inclination to the lamellae they examined for a syrup flotation tank. Reali and Marchetto (2001) reported that varying the angle of the lamellae between 60 and 70 degrees had minimal effect on the performance of the flotation tank.

Figure 1b depicts the geometry of the tank and the planes used for a detailed flow analysis. The horizontal plane HP-A has been positioned 87 cm above the ground and coincides with the upper edge of the lamella pack, while planes IP-A and IP-B are inclined at 60 degrees to the horizontal plane and have been placed between lamellae 3 and 4 and lamellae 13 and 14, respectively. To economise computer resources, only one half of the tank was simulated due to its symmetry plane, although despite this, the findings are represented with an identical replica relative to the symmetry plane. For a more comprehensive explanation of the results, the air concentration contours and water velocity vectors will be presented together.

Table 1 summarises the cases that were analysed for this research work. The first three cases were tested by Lundh et al. (2000, 2001; 2002) in their pilot plant (without lamellae), and the authors' designations (M19, M21, and M17) have been retained here. On the basis of the preceding cases, the MQ25 case was defined by establishing a higher raw water flow rate, which allowed for an analysis of L-DAF tank operation with very high HL (about 30 m/h). When these cases were simulated in the tank using lamellae, the prefix L- was added, e.g. L-M21. The total flow (Q_T) to be treated in the DAF tank was equal to the sum of the raw water flow (Q) and recycle flow (Q_r), where bubbles were

Table 1 Water velocity and air volume fraction values

Case	Q_T (m^3/h)	HL (m/h)	C_{cz} (ml/l)	α_A	V_r (m/h)
M19	11.0	11.8	5	0.052	5.0
M21	16.5	17.7	6	0.062	7.5
M17	22.0	23.7	6	0.049	9.9
MQ25	27.5	29.6	8*	0.053	12.5

*The C_{CZ} in the MQ25 case was estimated based on the values measured in the other three cases

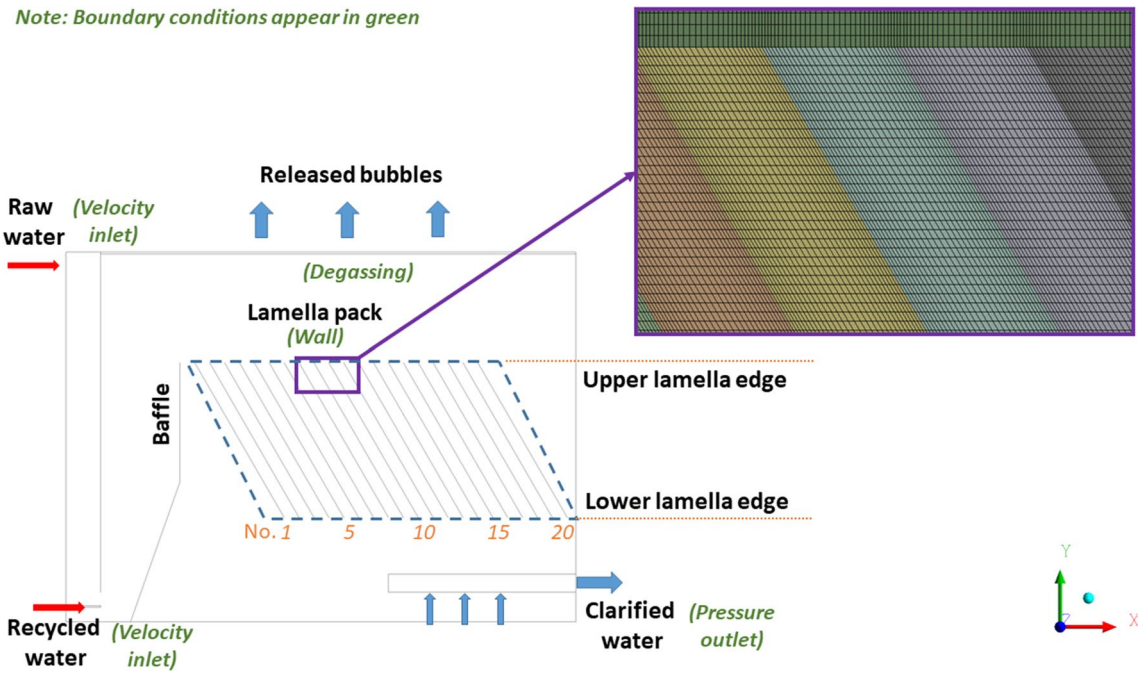

Fig. 2 An example of the 32M elements mesh in the lamella region seen in the symmetry plane as well as a few key terms used throughout the paper

introduced (see Fig. 2). In all cases, the recycle flow rate was set at 10% of raw water flow rate, and hydraulic loading (HL) was calculated using the total flow rate and separation zone surface area (0.93 m^2).

The average contact zone concentration (C_{cz}) determined by Lundh et al. (2001) can also be found in Table 1, along with the velocity of the water-bubble mixture in the recirculation flow injectors (V_r) and the volume fraction of air in the latter (α_A), which was calculated from the C_{cz}. The values of HL and CZ concentration (C_{cz}) in each case were then used to make the velocity (vectors and vertical Y-component) and air concentration dimensionless, respectively. The area of the main inflow required to calculate the velocity of the raw water flow was 0.07 m^2.

It is common knowledge that the bubble diameter employed in simulations has a substantial effect on the resulting flow behaviour within DAF tanks (Echeverri and Rein 2007; Emmanouil et al. 2007; Bondelind et al. 2010b; Hlukhov et al. 2022). Hlukhov et al. (2022) showed that flow behaviour varies depending on whether bubble diameters are greater or less than the so-called critical diameter, which corresponds to bubbles with a rising velocity equal to HL. In this work, critical-diameter (D_c) values in cases M19, M21, M17, and MQ25 are close to 77, 95, 110, and 123 µm, respectively. Using bubbles with diameters greater than the critical diameter in simulations caused the bubble blanket to remain clearly above the lamella pack, resulting in conditions under which the lamellae simply distribute and guide the clarified water to the outlet. Smaller than critical-diameter bubbles that are entrained within the lamellae by the water flow were chosen to explore the operating mechanism of the lamellae. In the three studies conducted, it was deemed reasonable to utilise bubbles of a single diameter, although the influence of bubble coalescence on the flow within the lamellae will be discussed.

In the first study, which analysed the effect of introducing lamellae into the DAF tank, the same bubble diameters were employed in the M19 and M21 cases as in the previous work without lamellae, i.e. 67 and 90 µm, respectively. Hence, it was possible to make a direct comparison between cases with and without lamellae under conditions when the flow without lamellae exhibits the features of a short-circuit (M19) and a stratified flow (M21). In the second study, detailed research of lamella performance was conducted employing a bubble diameter of 67 µm in the M21 case, because flow characteristics between the lamellae were more pronounced and clearer to describe. In the third study, simulations of the cases under consideration (M19, M21, M17, and MQ25) were also carried out with a bubble diameter of 67 µm, in order to clearly observe the effect of HL on L-DAF performance.

Mathematical model and resolution

Two multiphase models were analysed in the previous study without lamellae, namely the Euler-Euler (Ishii and Mishima 1984) and Mixture (Manninen et al. 1996) models, and both proved to provide very similar results. In this work, the Mixture model, which is computationally less expensive and has been successfully used by other authors (Emmanouil et al. 2007; Lakghomi et al. 2012; Satpathy et al. 2020), will be utilised for the simulations. The continuity, momentum, and volume fraction equations take the following form:

$$\frac{\partial \rho_m}{\partial t} + \nabla\left(\rho_m \vec{v}_m\right) = 0 \tag{1}$$

$$\frac{\partial \rho_m \vec{v}_m}{\partial t} + \nabla \cdot \left(\rho_m \vec{v}_m \vec{v}_m\right) = -\nabla p + \nabla \cdot \left[\mu_m\left(\nabla \vec{v}_m + \nabla \vec{v}_m^T\right)\right] + \rho_m \vec{g} - \nabla \cdot \left(\sum_{k=1}^{n} \alpha_k \rho_k \vec{v}_{dr,k} \vec{v}_{dr,k}\right) \tag{2}$$

$$\frac{\partial \alpha_p \rho_p}{\partial t} + \nabla\left(\alpha_p \rho_p \vec{v}_m\right) = -\nabla \cdot \left(\alpha_p \rho_p \vec{v}_{dr,p}\right) + \sum_{q=1}^{n} \left(\dot{m}_{qp} + \dot{m}_{pq}\right) \tag{3}$$

where $\vec{v}_m = (\sum_{k=1}^{n} \alpha_k \rho_k \vec{v}_k)/\rho_m$ is the mass-averaged velocity, $\rho_m = \sum_{k=1}^{n} \alpha_k \rho_k$ is the mixture density, μ_m is the mixture viscosity, α_k is the volume fraction of phase k, and n is the number of phases. Drift velocity $\vec{v}_{dr,k} = \vec{v}_k - \vec{v}_m$ is used to close the conservation equation and is related to relative (or slip) velocity $\vec{v}_{kq}$ via the following equation:

$$\vec{v}_{dr,k} = \vec{v}_{pq} - \sum_{k=1}^{n} c_k \vec{v}_{kq} \tag{4}$$

where $\vec{v}_{kq}$ is the velocity of phase k relative to phase q and $c_k = \alpha_k \rho_k / \rho_m$ is the mass fraction of phase k. In accordance with (Manninen et al. 1996), the form of the relative velocity is given by:

$$\vec{v}_{pq} = \frac{\tau_p\left(\rho_p - \rho_m\right)}{f_{\text{drag}} \rho_p} \vec{a} - \vec{v}_t \tag{5}$$

where $\vec{a}$ is the secondary phase acceleration, τ_p relaxation time of a bubble, $\vec{v}_t$ is the turbulence contribution to the velocity, and f_{drag} is the drag function. In the previous study, it was determined that Schiller–Naumann drag law is suitable for DAF applications, and it is going to be utilised to calculate the exchange of momentum via drag between water and air bubbles. The drag function of Eq. (1) is defined as follows: $f_{\text{drag}}=1+0.15\text{Re}_p^{0.687}$ (for $\text{Re}_p \leq 1000$).

As regards boundary conditions, the pilot tank has a symmetry XY-plane that passes through the middle of the tank; therefore, the symmetry condition was used to split

the tank in two halves. Recycled flow injectors with 5-mm internal diameter (in the form of squares of equivalent area) and the freshwater inlet were modelled as a velocity inlet (see Fig. 2). Lundh et al. (2002) did not quantify the turbulence intensity at the inlets of the two flows, hence a value of 5% was taken into consideration. Clarified water outlet was modelled as a rectangular pipe—as other authors (Bondelind et al. 2010a; Rodrigues and Béttega 2018) did—with evenly distributed squares (20 per pipe) and in which a pressure outlet condition was set. Lamellae were modelled, like the rest of the tank walls, as solid surfaces with the no-slip condition. The air mass sink term proposed by Ta et al. (2001) for the degassing condition was implemented via a user-defined function. More detailed explanation on the boundary conditions can be found in the previous study without lamellae carried out by the authors.

Hlukhov et al. (2022) demonstrated that the solutions obtained via Reynolds-averaged Navier-Stokes (RANS) steady-state simulations were very similar to those obtained by sufficiently long flow-time transient simulations that reached quasi-steady solution. Therefore, steady-state RANS simulations were carried out in this study. The two-equation realisable k-ε model with standard wall functions was used to account for turbulence, as it has been by numerous other authors (Kwon et al. 2006; Amato and Wicks 2009; Bondelind et al. 2010b, a; Lakghomi et al. 2015). In the iterative calculation, pressure, velocity, and volume fraction were solved in a coupled manner, followed by the resolution of turbulent kinetic energy (k) and dissipation rate (ε) that were solved sequentially in the case of each iteration. The mathematical model was solved using the commercial code ANSYS Fluent 2020R1.

In the previous study without lamellae, an estimation of the discretization error based on Richardson Extrapolation proposed by Celik et al. (2008) was carried out. The grid convergence index (GCI) of the average air fraction in the tank was 4.7% for the 5-million mesh that was used in the study, concluding that it was fine enough to predict the flow in the DAF tank with low numerical uncertainty.

In the case of the present L-DAF, three meshes of different refinement levels in the lamella region were evaluated, the element distribution in the CZ remaining unchanged from the prior study. By increasing the number of inter-lamella elements from 15 to 20 and 30 elements, meshes with a total of 13, 24 and 32 million elements were created. The refinement factor (RF) was only applied to the inter-lamella spacing because it is considered the most critical region in an L-DAF. Nevertheless, as the mesh is conformal this refinement is projected to the elements above and below the lamella pack (see Fig. 2). The RF value between the coarse and medium mesh was equal to 1.3, and the RF between the medium and the fine mesh was equal to 1.5. The number of elements distributed along the length of the lamella was sufficiently high so as not to influence the flow resolution. The mean values of mixture velocity and air fraction were evaluated in the two inter-lamella channels that are discussed in detail in the next section. Thirty elements were determined to be sufficient to define the flow characteristics between lamellae, although some regions of especially high air concentration and velocity gradients were found very close to the lamella surface, which would require an extremely fine meshing to be accurately resolved.

Results and discussion

Firstly, the hydrodynamic behaviour of the DAF tank with and without lamellae under distinct operating conditions is analysed. The impact of HL on the flow within the tank with lamellae (L-DAF) is also examined, and the bubble removal efficiency is calculated for each case. Subsequently, the structure of the flow in an L-DAF is analysed in depth utilising multiple planes that help comprehend its three-dimensional nature. Research was conducted into the mechanism by which bubbles enter between the lamellae, but do not pass through them, and ultimately exit at the top.

The results shown in all the figures come from steady-state RANS simulations; therefore, displayed air concentration and water velocity stand for mean values of both magnitudes. As noted before, the air concentration contours and velocity vectors that are presented in this section have been adimensionalized using C_{cz} and HL, respectively. The simulation represented in each figure is labelled as MXX_YY-ZZ, where MXX refers to the name of the experiment, YY is the value of the hydraulic load, and ZZ corresponds to the diameter of the bubbles.

Differences in hydrodynamic behaviour between a DAF and an L-DAF

In this first study, the comparison of the results was carried out in the symmetry plane, as is customary in CFD studies of DAF tanks (Echeverri and Rein 2007; Amato and Wicks 2009; Bondelind et al. 2010b; Lakghomi et al. 2012; Satpathy et al. 2020).

Figure 3 shows the air concentration contours and water velocity vectors in the symmetry plane in the M19 and M21 cases with and without lamellae. Flow in the M19 case with 67-micron bubbles and no lamellae (Fig. 3a) exhibits clear short-circuit characteristics, with the main current leaving the CZ and heading directly into the outlet pipes, thus carrying a considerable quantity of bubbles into it. Similar result has also been observed, but with a much more pronounced short-circuit in the cases M17 and MQ25 with the same bubble diameter. In contrast, the flow in the M21 case with 90-micron bubbles and no lamellae (Fig. 3c) is

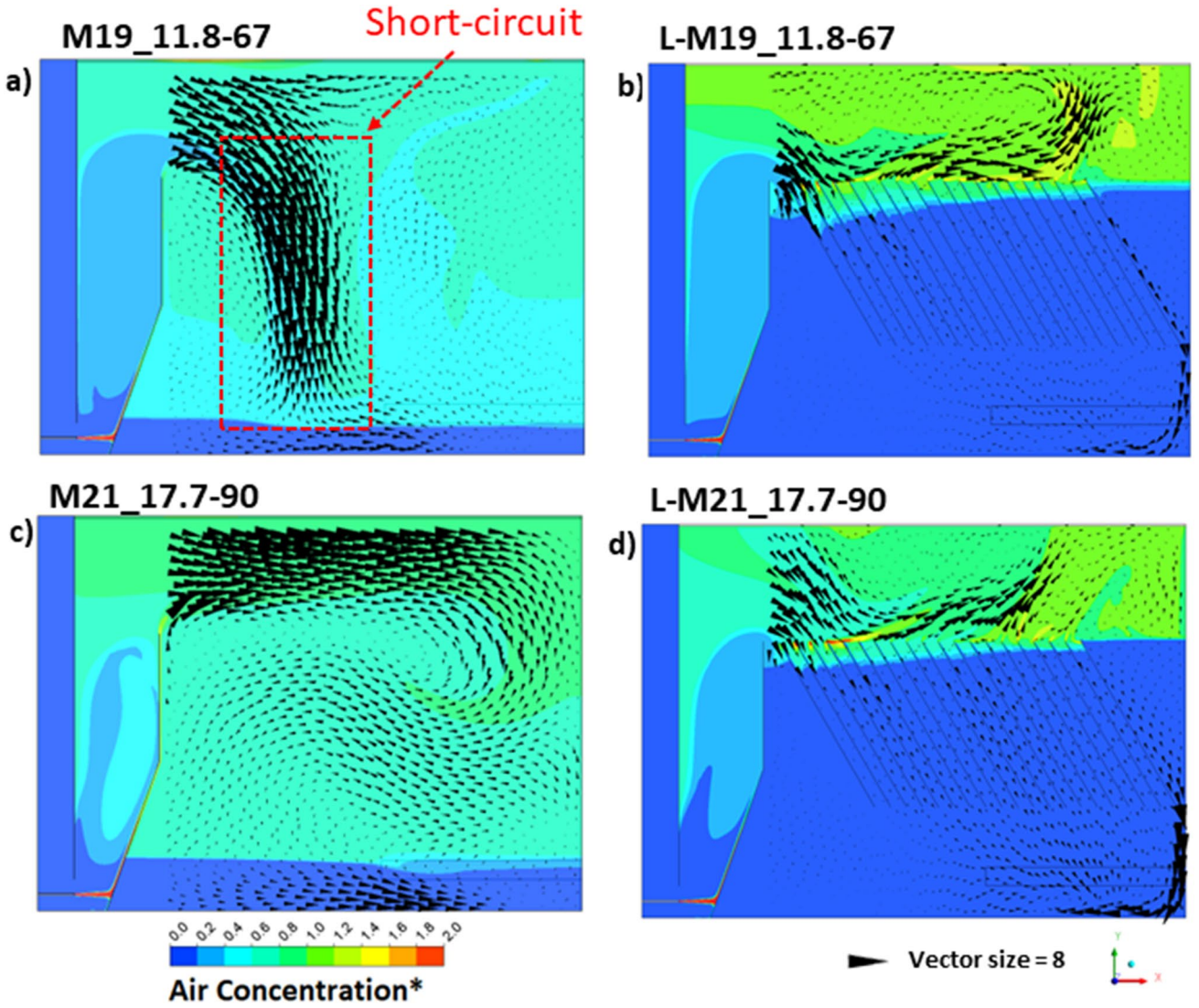

Fig. 3 Dimensionless air contour and dimensionless water vectors in the symmetry plane in the M19 (**a**) and L-M19 (**b**) cases with 67 µm bubbles; M21 (**c**) and L-M21 (**d**) cases with 90 µm bubbles

substantially stratified. The main current leaving the CZ has a higher concentration of air, and therefore a lower density, than the water below it. Consequently, water flows parallel to the surface until it reaches the far end wall, where it turns downwards and reverses direction. Under these conditions, the bubble blanket remains above the orifices of the outlet pipes and few bubbles escape through them.

Figure 3b, d demonstrates the fact that the introduction of lamellae eliminated the flow characteristics that prevailed in the absence of lamellae, namely the short-circuit in the M19 case and the stratified flow in the M21 case. Both cases produce a flow characterised by a shallower, albeit higher bubble concentration blanket, extending from the free surface to a few centimetres below the upper lamella edge. The clarified water passes through the lamellae and enters the outlet pipes below the bubble blanket. These flow characteristics in the L-DAF tank have been visualised through transparent walls in a number of pilot plants. Fang et al. (2009) highlighted the compactness of the bubble blanket and the sharpness of its border with the clarified water, whereas Hedberg et al. (1998) emphasised the steep density gradient between the two zones. In simulations of the L-M19 and L-M21 cases, the density difference between the bubble blanket and the clarified water was determined to be roughly 5 kg/m^3. This difference is considerably higher than the difference between the two opposing flows in the stratified flow case M21 (Fig. 3c), which was estimated by Lundh et al. (2000) to be 2 kg/m^3. By having a Richardson number (Ri) considerably higher than one ($R_i \approx 55$), these authors determined that the stratification is quite stable considering this

density difference. A characteristic identified in the L-M19 and L-M21 simulations demonstrates the impact of having a significantly higher density difference when placing the lamellae in the SZ (Fig. 3b, d). A portion of the current that exits the CZ closest to the baffle turns downwards and passes through the space between the baffle and the first lamella, although its reduced density in comparison to the clarified water beneath it prevents it from penetrating.

The mechanism by which the lamellae retain the bubbles and only allows the clarified water to pass towards the outlet pipes is not evident when analysing only the flow in the symmetry plane shown in Fig. 3b, d and will be analysed in detail in the next section. Nevertheless, a significant phenomenon that the presence of the lamellae produces in the current that leaves the CZ was able to be observed. A substantial portion of the current directed at the lamellae flows horizontally over them towards the far end wall of the SZ. The current then changes its direction above the final lamellae and returns in a layer just beneath the free surface, albeit at a substantially slower velocity. Hence, the distance the bubbles must travel to reach the surface is considerably shorter than in conventional DAF, which facilitates bubble removal. Efficiency was evaluated in the four cases under consideration and found to be significantly better in cases with lamellae. The amount of air that escapes via the outlet pipes was lowered from 16% in M19 to 0.2% in L-M19. In the M21 case, the amount of air entrained to the outlet was relatively small (0.9%) compared to M19, although after including the lamellae, bubble removal was nearly complete.

The effect of the hydraulic loading on L-DAF performance was analysed by comparing the results of the four cases shown in Table 1, ranging from 11.8 to 29.6 m/h and simulated with 67 µm bubbles. Figure 4 shows the water velocity vectors and air concentration contours in the symmetry plane for the four cases examined. As can be seen, the most significant changes occur in the flow between the lamellae, specifically in the depth that the bubble blanket reaches between them, which increases as HL rises. However, the increase in blanket depth is not homogeneous, but rather, more pronounced in the first lamellae through which more flow passes than in the last ones, in which there is a greater concentration of bubbles and, therefore, a greater difference in density from the clarified water below.

As shown in Fig. 4, when HL is greater than or equal to 23.7 m/h, a short-circuit is created and the current transports a portion of the bubbles that enter between the first five lamellae up to the lower lamella edge, where they eventually escape through the outlet pipes (see Fig. 4c, d). In contrast, even at these flow rates, the bubble blanket in the last lamellae is especially high, and no bubbles escape through the lower lamella edge. Theoretically, the design could be improved by adding a perforated plate beneath the lamella pack, as Hedberg et al. (1998), Fang et al. (2009), and Azevedo et al. (2018) did. In the CFD L-DAF tank model, the perforated plate could be modelled as a "porous jump condition", and this research would allow the pressure drop required to guarantee a more uniform flow distribution between the lamellae to be determined and further reduce the number of bubbles reaching the outlet pipes at higher HLs.

In contrast to what occurs between the lamellae, the flow near the free surface is similar in all four cases and characterised by a very low velocity current in the direction of the CZ, even when the L-DAF is operating at its maximum HL of 29.6 m/h. This result suggests that, due to the lamellae, the part of the bubble blanket closest to the free surface and foam layer above it are shielded from disturbances occurring in the bottom part of the tank near the outlet pipes. This conclusion is consistent with the findings of Fang et al. (2009) and Azevedo et al. (2018), whereby lamellae increase bubble blanket stability.

Figure 5 contrasts the bubble removal efficiency of the tank operating with the four HLs under consideration, as well as the results obtained without lamellae. With the two lowest HLs, which are high in terms of the range of conventional DAFs, the percentage of air escaping with the clarified water is considerably below 1% with lamellae, but reaches values as high as 16.4 and 38.6% without them. With the two highest HLs, where bubbles were observed leaking through the first lamellae (Fig. 4), bubble removal efficiency remains above 90%. These values exceed SS removal efficiency published in the literature for L-DAF tanks. For example, Fang et al. (2009) achieved (also utilising a perforated plate) turbidity removal of around 95% with HL of 18 m/h, whereas Jokela and Lepistö (2014) achieved an 85% decrease in TSS with HL of 17.5 m/h. Nonetheless, the qualitative comparison of the L-DAF results analysed with those experimentally obtained by Hedberg et al. (1998) in their pilot plant (see Fig. 6) demonstrates that bubble removal efficiency can be used to evaluate tank performance and to predict trends regarding the effect of HL on the latter.

The length, angle, and inter-lamella spacing values of the L-DAF analysed are comparable to those used by Hedberg et al. (1998) in their experiment Nº 2. To qualitatively compare the results of this study with those experimentally obtained by Hedberg et al. (1998), the percentages of escaped air from the L-DAF in Fig. 5 are shown in Fig. 6a in terms of hydraulic loading HL_{LA}, which is determined by dividing the overall flow rate (Q_T) by the horizontal lamella area (HLA). Although Hedberg et al. (1998) worked with a lower overall flow rate, their plant had a smaller HLA of 0.3 m^2 compared to the L-DAF tank used in this research, which had an HLA of 0.7 m^2, and their turbidity results as a function of HL_{LA} are shown in Fig. 6b. Although the NTU values and the percentage of escaped air are not

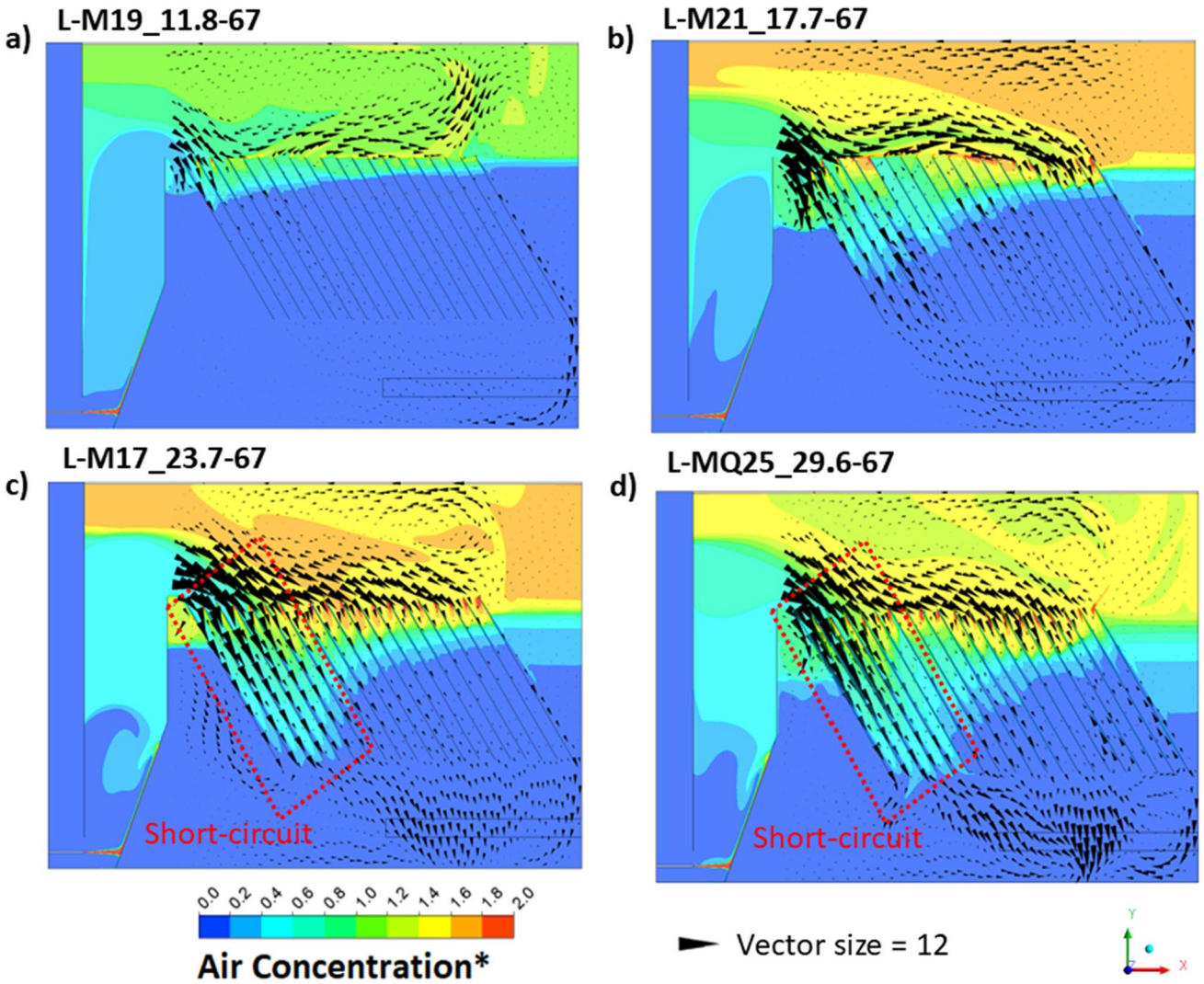

Fig. 4 Dimensionless air concentration and dimensionless water velocity vector contours in the following cases: L-M19 (**a**), L-M21 (**b**), L-M17 (**c**), L-MQ25 (**d**)

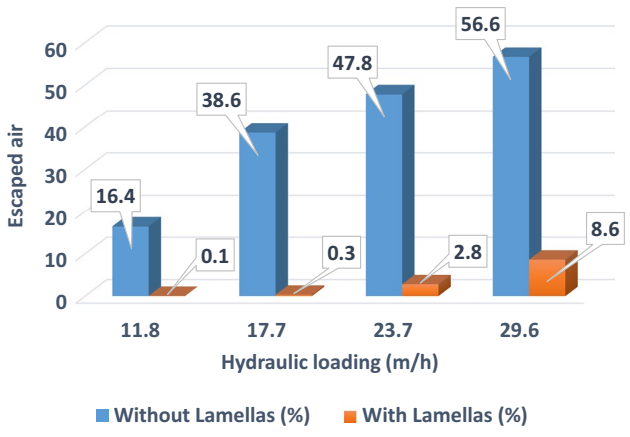

Fig. 5 Percentage distribution of escaping air through the outlet pipes vs entering air for various hydraulic loadings with and without lamellae

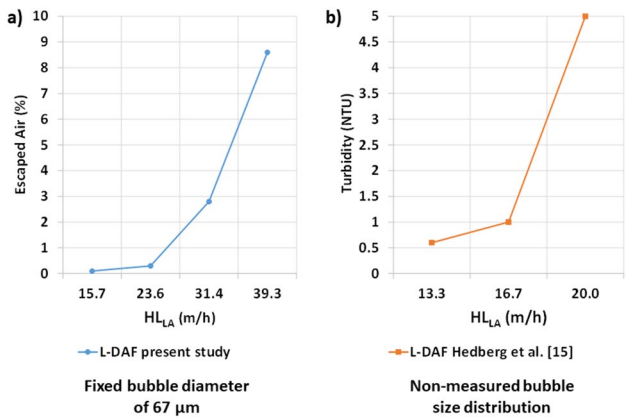

Fig. 6 Comparison of escaped air curve vs HL of the present study (**a**) and NTU versus HL of Hedberg et al. (1998) (**b**)

directly comparable, they are both related to separation efficiency, with a high NTU value indicating a low separation efficiency.

As can be seen in Fig. 6, the curve obtained for escaped air resembles the turbidity curve obtained by Hedberg et al. (1998). In both instances, the slope of the curve changes significantly from a specific value of HL_{LA}. Hedberg et al. (1998) found that as HL_{LA} increased, more bubbles escaped from the tank, leading to a significant increase in turbidity. In the L-DAF analysed, the slope change begins at an HL_{LA} of 31.4 m/h (HL = 23.7 m/h), precisely when the bubbles begin to cross the lower lamella edge and are dragged to the outlet pipes (see Fig. 4c). Consequently, it is evident that the bubble removal efficiency analysis of an L-DAF tank performed using a two-phase (water-bubble) CFD model can also be used to determine an estimate of the HL at which a significant decline in the quality of clarified water can occur.

Although the study on the effect of hydraulic loading has been conducted with 67-micron bubbles, it is expected that any bubble size below the critical diameter will yield similar results. If bubbles with a diameter smaller than 67 microns were used, the total amount of escaped air would be higher and vice versa for bubbles larger than 67 microns but smaller than the critical diameter. Further information regarding flow behaviour with different bubble diameters can be found in Hlukhov et al. (2022).

Detailed analysis of lamella operation

Extensive computational analysis of the L-DAF tank under various operating conditions revealed that the flow between lamellae has a complex three-dimensional structure. This structure cannot be viewed through transparent walls and therefore could not be described in the pilot plant studies conducted to date, as to properly describe the flow characteristics require going beyond the symmetry plane analysis performed in the previous study. In order to visualise and describe the flow patterns in the L-DAF tank separation zone, multiple planes were generated and analysed (Figs. 9 and 10), and the L-M21 case with 67 µm bubbles is shown and examined since the flow features between the lamellae are more prominent, making the explanation clearer.

Figure 7 shows the air concentration contour together with the water velocity vectors in the symmetry plane so that they can be compared to those of the L-M21 case with 90 µm bubbles described previously (Fig. 3d). On the one hand, it can be seen that the flow maintains the same fundamental characteristics regardless of the lower buoyancy of the 67 µm bubbles. The blanket contains a greater concentration of bubbles and, hence, a lower density than the clarified water beneath it. The current exiting the CZ and passing through the space between the baffle and the first lamella carries bubbles deeper, although its lower density prevents

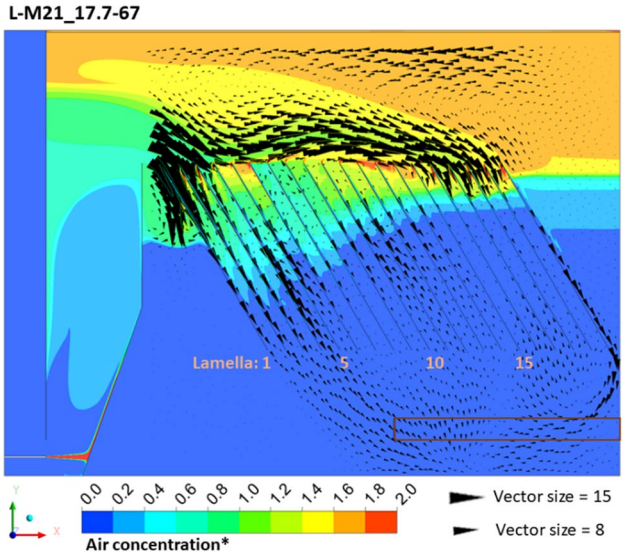

Fig. 7 Dimensionless air concentration contour and dimensionless water velocity vectors in the symmetry plane of the L-M21 case with 67 µm bubbles

it from penetrating the clarified water once more. The lesser buoyancy of the bubbles also causes them to be dragged deeper between the lamellae, and even more so between the lamellae that are closer to the separating baffle.

On the other hand, three characteristics of the flow between the lamellae that are also in evidence with 90 µm bubbles but are not visualised in Fig. 3d can be identified more clearly. Firstly, there are downward currents on the lamella top side, as indicated by the greater vectors near the lamellae that exist in both the bubble blanket and the clarified water underneath. These currents are described in further depth using Fig. 10 and Fig. 12 in later paragraphs. Secondly, although it is only apparent in Fig. 7 between a few lamellae (e.g. 6–7 and 7–8), there are ascending currents at the bottom side of the latter. These currents, which are driven by the accumulation of bubbles that reach these surfaces by flotation, are shown more clearly in Figs. 9, 10, and 12 that will be explained later. Thirdly, the horizontal current above the lamellae towards the opposite wall carries the bubbles emerging from the lamellae to the lamellae downstream. This characteristic is especially evident in Figs. 9 and 10 that will be discussed below.

Figure 8 shows the percentage of total water flow (Q_T) passing through each pair of lamellae, the space between the baffle and the first lamella (P1), and the space between the last lamella and the back wall (P2). Due to its larger dimensions, a greater flow rate passes through the latter, whereas a flow rate comparable to that between two lamellae flows through the former. The histogram reveals that the flow distribution between lamellae is not uniform. Significantly more flow passes through the first third of the lamellae,

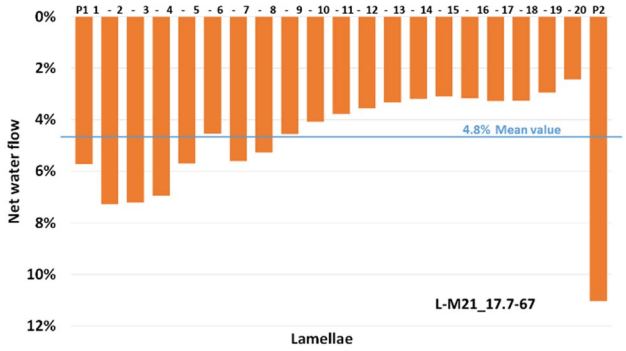

Fig. 8 Distribution of net water flow between the lamellae. Percentage values are in reference to the total net flow through the SZ section. The blue line marks the average value

which explains why bubbles are dragged at a greater depth and the border of the blanket is closer to the ground, as shown in Fig. 7. This uneven flow distribution in which the first lamellae are favoured also explains the increased risk of bubbles passing beyond these lamellae and exiting through the outlet pipes, as was observed when the treated flow rate (Q) was raised (see Fig. 4).

Figure 9 shows the three-dimensional nature of the flow in the L-DAF tank separation zone, particularly between the lamellae. The contours of the vertical component (*Y*-direction) of the water velocity and the air concentration are shown in the HP-A plane, located at the upper lamella edge, inside the bubble blanket. In addition to the *X*-direction, the flow characteristics vary significantly in the transverse *Z*-direction, allowing a distinction to be drawn between regions with clearly differing water velocities and bubble concentration. Firstly, it is noteworthy that in Fig. 9a there are large regions where the water flow is upward, bringing bubbles out from the lamellae. As can be seen in Fig. 9b, bubble concentration in these regions is typically greater than in regions where the water flow descends and drags bubbles within the lamellae. Figure 9b also reveals that the upper border of the lamellae (further from the CZ) contains a substantially higher concentration of bubbles. This increased concentration of bubbles is caused by the horizontal current passing over the lamellae, which drags the bubbles emerging from between the lamellae (see Fig. 7).

In Fig. 9a, b, the lamella edges can be distinguished by the narrow regions of ascending velocity and high air concentration along the transverse *Z*-axis. When the flow between the lamellae in various *XY* planes is analysed in detail (Figs. 11 and 12), it will be shown that the aforementioned characteristics are those of the flow produced by the buoyancy of bubbles towards the bottom side of the lamellae, which were previously seen in the symmetry plane (Fig. 7). However, the upward velocity regions, where water (with bubbles) flows out of the lamellae, extend beyond the surface of the lamellae and occupy a substantial portion of the space between some of them. It was found that there are regions of upward flow between all lamellae, despite the fact that the net flow of water across all pairs of lamellae is downward, as shown in Fig. 8.

The fact that the regions with the highest upward velocity are next to those with the highest downward velocity is a crucial aspect of the flow between the lamellae shown in Fig. 9a. The details of the flow that result in this characteristic were analysed by employing inclined planes parallel to the lamellae, and it was found that this plays an important role in the mechanism by which the lamellae prevent bubbles from flowing through and eventually allows them to escape via their upper edge. Figure 11 shows the water velocity vectors as well as mean air concentration contours in the IP-A and IP-B planes, which are located between lamellae 3–4 and 13–14 (see Fig. 1b), respectively. In both planes, it can be observed that a bubble-rich current entering between the lamellae with significant velocity (between 5 and 15 times

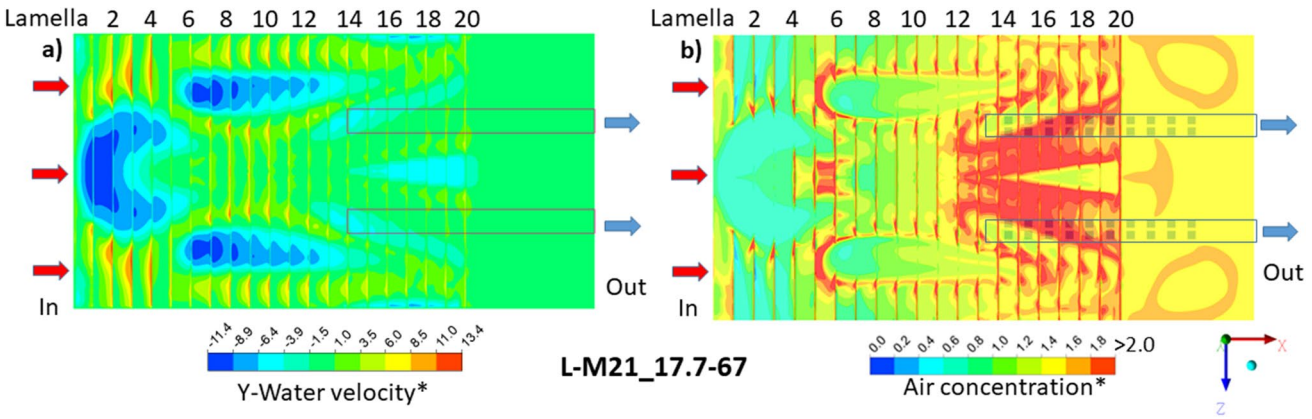

Fig. 9 Contours of the Y-component of the dimensionless water velocity and dimensionless air concentration in the HP-A (**a**–**b**) plane in the L-M21 case. At some points close to the upper side of the lamella, the concentration can be within the range of 2–6

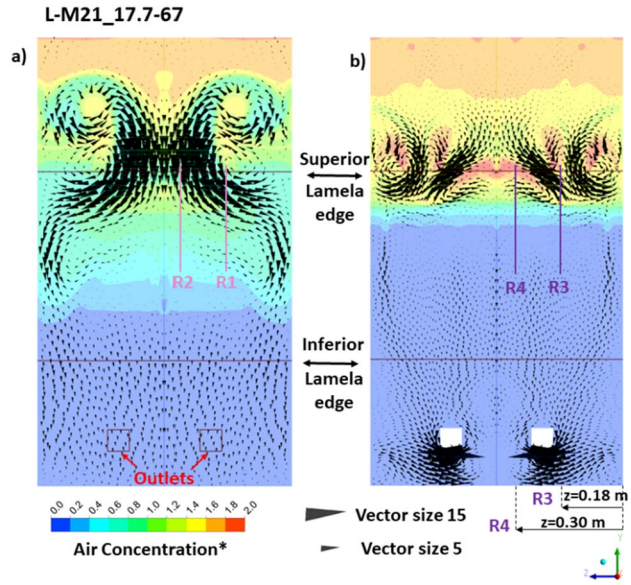

Fig. 10 Dimensionless water velocity vectors and dimensionless air concentration contours in the IP-A and IP-B planes. In the figures, the lamella borders along with the intersections with the R1-4 planes specified in Fig. 9 are indicated. Planes R1 and R3, as well as planes R2 and R4, have the same Z-coordinate value; see (**b**)

the HL) cannot continue due to its lower density and reverses direction in the plane examined, exiting the lamellae and dragging bubbles with it. This is the same mechanism that prevents the current leaving the CZ and passing through the gap between the baffle and the first lamella from penetrating the clarified water (see Figs. 3b, d and 7).

Even though the aforementioned mechanism is in evidence between all lamellae, a comparison of the IP-A (Fig. 10a) and IP-B (Fig. 10b) planes reveals the most significant differences between the flow structures in the first lamellae, where the water flow is higher (Fig. 8), and the last lamellae, where there is a higher concentration of bubbles at their upper edge (Fig. 9b). In the IP-A plane (Fig. 10a), the current originating directly from the contact zone (see Fig. 7) reaches the lamellae at significant velocity at the centre of the plane. Shortly after entering the lamellae, the existing density gradient forces the current to rotate, and a portion of it leaves the lamellae. However, a significant portion of the current is directed towards the tank walls and becomes attached to them, dragging the bubbles deeper, albeit not reaching the lower edge of the lamellae. In the IP-B plane (Fig. 10b), the current arrives after passing over multiple lamellae and entrapping a substantial number of bubbles (Fig. 9b). This current enters at a lower velocity

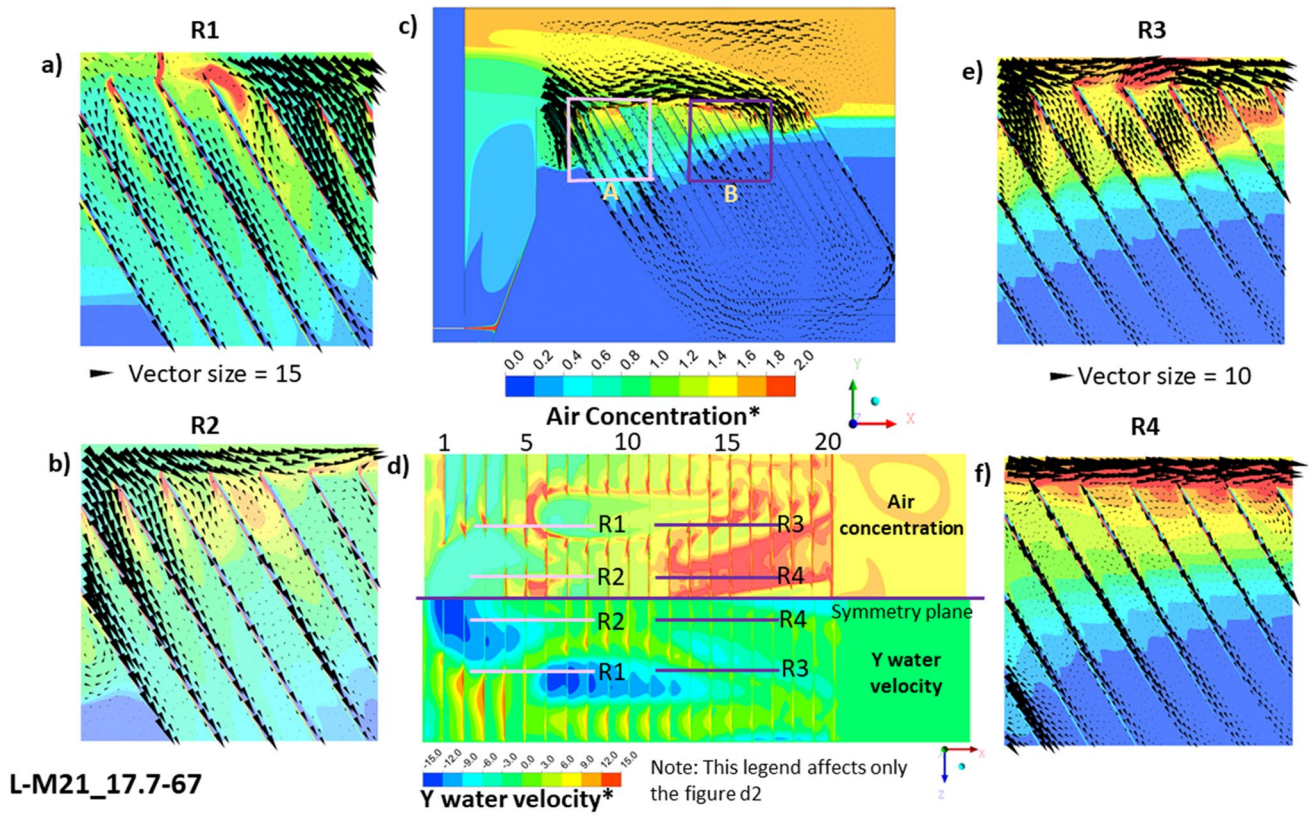

Fig. 11 Dimensionless air contours and dimensionless water vectors in the L-M21 case in the symmetry plane (**c**) and the HP-A plane (**d**). Views R1 (**a**) and R2 (**b**) are located in zone A, while views R3 (**e**) and R4 (**f**) are located in zone B

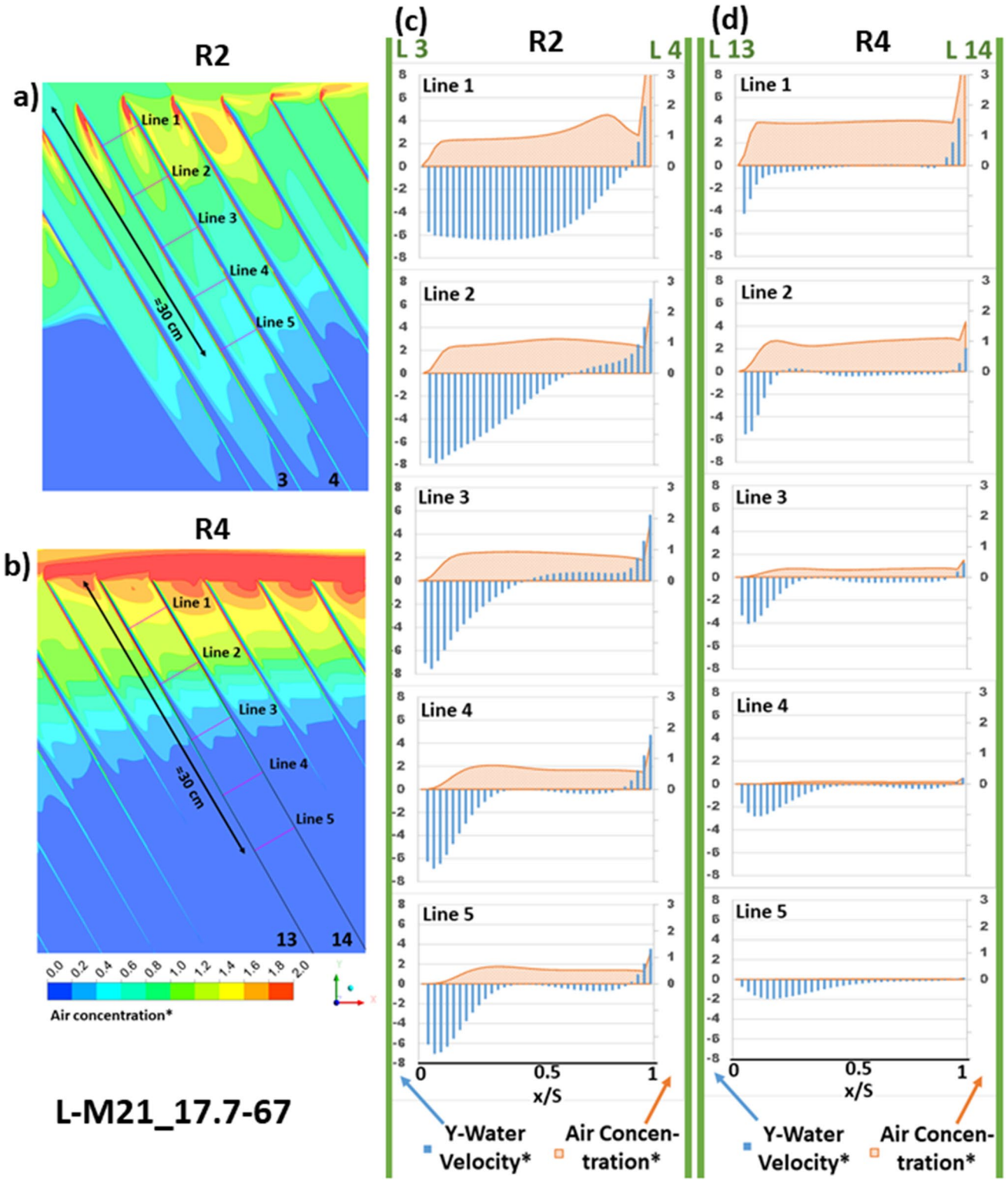

Fig. 12 The position of the five lines in planes R2 (**a**) and R4 (**b**) on which the Y-component profiles of the adi-dimensional water velocity and dimensionless air concentration between lamellae 3 and 4 (**c**) and lamellae 13 and 14 (**d**) have been plotted

than in the IP-A plane and encounters a significantly higher density gradient than in the IP-A plane; consequently, it penetrates much less between the lamellae and exits the latter while dragging the bubbles along with it. Under the bubble blanket, water velocity is predominantly downwards and behaves comparable to a plug flow in both planes.

Once the transverse currents (in the Z-direction) at the top region of the lamellae have been described, the flow characteristics between the lamellae in the direction towards the outlet pipes (XY-plane) can then be properly analysed. These features are shown in Fig. 11 in four planes defined in two separate zones (A and B) and in two distinct transverse coordinates (Z). Zone A is positioned between lamellae 1 and 7, and the defined planes R1 and R2 intersect with the IP-A plane positioned between lamellae 3 and 4 (Fig. 10a). Zone B is situated between lamellae 9 and 16, hence the defined R3 and R4 planes intersect with the IP-B plane positioned between lamellae 13 and 14 (Fig. 10b). In the four planes shown in Fig. 11, the two currents attached to the lamella surfaces observed in Fig. 7 and Fig. 9 are more evident, namely the descending current attached to the top side of the lamella and the ascending current attached to the bottom side (see also Fig. 12). However, the flow characteristics vary in different regions depending on the velocity and concentration of the current entering between the lamellae.

As shown in Fig. 11, in regions where the current enters at high velocity between the lamellae, it occupies practically the entire width between them, as observed in the R1 plane (between lamellae 6–8), the R2 plane (between lamellae 1–4), and the R3 plane (between lamellae 9–16). However, it was ascertained that further downstream the descending current only persists near the upper surface of the lamellae, and the water velocity is reduced throughout the remainder of the width. This substantial change in flow is as a result of the bubble-rich current's inability to move forwards due to its lower density, causing it to turn perpendicular to the R1–4 planes (see Fig. 10). In the R3 plane, near the upper edge of the lamellae, the change occurs abruptly due to the high bubble concentration (see also Fig. 10b), whereas in the R1 and R2 planes the density change is more gradual and the descending current occupies a significant proportion of channel width at greater depth (see also Fig. 10a). In contrast, in the R4 plane, bubble concentration above the lamellae is especially high, and relatively little current travels in the direction of the outlet pipes (see also Fig. 10b). In any case, Fig. 11 also demonstrates that, regardless of the properties of the current that enters between the lamellae, the previously indicated descending current occurs on the top side of all of them. These currents, unlike the first, are capable of breaking through the bubble blanket and eventually reach the clarified water below. The characteristics of these currents are discussed in further detail later in the analysis of Fig. 12.

As for the ascending currents below the bottom side of the lamellae, Fig. 11 shows that they are of small thickness, albeit easily discernible due to their high concentration of bubbles when they emerge at the top of the lamellae (see lamellae 3 and 4 in the R1 plane and lamellae 13, 14 and 15 in the R3 plane). Once these bubbles leave the lamellae, they are carried away by the horizontal current above the lamellae and, in some regions, reintroduced between consecutive lamellae (see lamella 5 in plane R1 and lamellae 14, 15 and 16 in plane R3). In locations where the current enters between the lamellae at high velocity, the ascending current is hindered and, in some cases, bubbles are reintroduced into the channel (see lamella 3 in plane R1, lamellae 3, 4 and 5 in plane R2—also in Fig. 12a—and lamellae 12 and 13 in plane R3).

Descending and ascending currents occurring on the top and bottom side of the lamellae can be seen in greater detail in Fig. 12. Air concentration contours are shown without velocity vectors in the R2 (Fig. 12a) and R4 (Fig. 12b) planes, so that their distribution within the lamellae of these regions can be better appreciated. Placed on these planes are also the lines whose profiles of air concentration and water velocity parallel to the lamellae are shown in Fig. 12c, d. The profile characteristics in the central portion of the lamella channel on the lines located in the bubble blanket are principally determined by the three-dimensional flow in the blanket, as reported earlier. For instance, the decrease in velocity observed in the middle section of the channel between lamellae 3 and 4 (lines 1–3) is caused by the turning of the current originating from the SZ, which cannot move forward due to its lower density (Fig. 10a). Similar decreases in air concentration are detected in the central portion of the channel between lamellae 13 and 14; line 2 is located in the region with a high concentration of bubbles near the upper edge of the lamellae, while line 3 is situated below (Fig. 8b). Consequently, it is not possible to analyse the evolution of the currents attached to lamellae as a two-dimensional flow evolving in the channels they form, as is done in lamellar settlers when employing 2- or 3-layer models (Borhan 1989; Reyes et al. 2022). Importantly, the aforementioned three-dimensional flow interacts with the currents moving along the lamellae.

As shown in Fig. 12a, b, the bubble-rich ascending current near the bottom side of the lamellae originates below the bubble blanket. The water beneath this still carries a limited number of bubbles that float to the lamellae. These bubbles form a thin layer that barely thickens until it reaches the bubble blanket, which contains a high bubble concentration. In the first lamellae, where strong currents from the CZ penetrate and push bubbles to greater depths, the ascending currents also begin at greater depth, thus obtaining greater thickness and higher velocity than in the lamellae that are closer to the far end wall (see lines 2–5 in Fig. 12c,

d). However, the same strong currents from the CZ drag a portion of the bubbles that rise attached to the lamellae and reintroduce them into the lamella channel. This phenomenon can be observed in regions of high air concentration around the upper borders of lamellae 2, 3, and 4. (Fig. 12a) and is also visible in the concentration profile of line 1 of plane R2, where a relative maximum is observed near the bottom side of lamella 4 in the downflow part (Fig. 12c). All these ascending current characteristics were determined without considering the possibility of bubble coalescence in the simulations. If this phenomenon had been accounted for, it is likely that the velocity and thickness of these currents would have been greater, although the general characteristics of the flow between and over the lamellae would not have changed significantly.

Finally, the results shown in Fig. 12 indicate that the descending current that develops on the top side of the lamellae begins at their upper edge. This current then increases and loses bubbles due to buoyancy as it progresses, generating an ever-thicker layer of clarified water linked to the wall. This evolution in the downward direction is evident in both the air concentration contours (see Fig. 12a, b) and water velocity and air concentration profiles in the channels between lamellae 3 and 4 (Fig. 12c) and between lamellae 13 and 14 (Fig. 12d). In the latter instance, where lines 4–5 lie below the bubble blanket, it is evident that these currents are able to break-through it and transport the clarified water below due to their higher density. The bubbles that are lost by these currents are transported away by the three-dimensional flow in the blanket, as deduced from all previous analyses. A portion of the bubbles is brought out from the top of the lamellae by this flow, while the remaining portion reaches the bottom side of the lamellae due to buoyancy, joins the ascending current, and ultimately exits above the lamellae through the aforementioned current. It has been demonstrated that this last-mentioned mechanism—the only one observed and described to date—is neither the sole nor the most essential means by which bubbles that enter between the lamellae exit over the lamellae and fail to reach the outlet pipes. The significant difference in densities that the lamellae let occur between the bubble blanket and clarified water also plays a key role that must be researched further in order to develop more effective L-DAF tanks.

Conclusions

The mechanism by which flat lamellae improve the performance of DAF tanks is commonly described as a two-dimensional flow in which bubbles (with flocs) accumulate on the bottom side and float off the top part of the lamellae. This reasoning is based on a (reverse) analogy with counter-current lamellar settlers and observation through transparent walls in pilot plants. The computer study conducted, however, revealed that the hydrodynamic structure of the flow in the separation zone of a DAF tank with lamellae is three-dimensional, complex, and conditioned by density difference. It was found that the lamellae generate a blanket with a high concentration of bubbles on top of the clarified water, so that the density gradient between the two zones is substantially greater than in a DAF tank with stratified flow but no lamellae, which prevents a bubbly current from passing through the lamellae by acting as a barrier. Therefore, the bubble-rich water currents channelled through the lamellae to the outlet pipes cannot progress, since their density is considerably lower than that of the clarified water below. Only descending currents that form on the top side of the lamellae and lose bubbles (increase in density) as they advance are capable of passing through the bubble blanket and transporting the clarified water beneath it.

Two mechanisms were identified that return bubbles which are unable to pass through lamellae to the region above them. On the one hand, the simulation results corroborate the existence of an ascending current near the bottom side of the lamellae, which is caused by the accumulation of bubbles rising to them by flotation. Simulations, on the other hand, demonstrated the existence of a second mechanism related to the density difference between the bubble blanket and the clarified water. Currents entering between the lamellae and reversing their direction transport a significant number of bubbles, which are afterwards evacuated from between the lamellae. These currents are stronger between the first lamellae, close to the CZ, and reach a greater depth than between the later lamellae, where the horizontal current over the latter transports the bubbles extracted by both mechanisms and increases the density gradient relative to the clarified water.

The influence of hydraulic loading on the performance and bubble removal efficiency of the L-DAF under consideration was examined. Major changes were observed in the flow between the lamellae, particularly in the depth of the bubble blanket between them, which increases as HL rises. However, the increase in blanket depth is not uniform, but rather, is more pronounced in the first lamellae through which more flow passes than between the last lamellae, where there is a higher density gradient relative to the clarified water. Once bubbles escape below the first lamellae, bubble removal efficiency begins to decline dramatically as HL grows. However, it remains greater than 90% at high HL—about 30 m/h, which is within the range of the high-rate DAF.

In conclusion, this study confirmed the ability of flat lamellae to significantly increase the HL at which DAF tanks can operate, but more importantly, it demonstrated that the performance improvement achieved with them is related to the density difference they cause to exist between the bubble

blanket and clarified water. It has therefore been proved that, in order to optimise performance of L-DAF tanks, it is necessary to analyse the effect of the lamella design parameters (length, angle, and distance between them), not only on the ascending currents produced by bubble flotation, but also on the density difference generated. The approach employed in this study, using CFD simulations of water and bubble flow within an L-DAF tank, is deemed suitable for such a parametric analysis.

Author contributions DH carried out CFD simulations, contributed in methodology, result discussion and writing and editing original draft; GSL was involved in conceptualization, methodology, result discussion, writing and editing original draft, and supervision; AR was involved in conceptualization, methodology, result discussion, manuscript review and supervision; JCR contributed in conceptualization, methodology, result discussion and manuscript review.

Funding This research has been partially funded by the Basque Government through the HAZITEK programme (Project ZL-2018/00582).

Data availability Some or all data models that support the findings of this study are available from the corresponding author upon reasonable request (CFD models, obtained numerical data, outputs, etc.)

Declarations

Conflict of interest The authors declare that they do not have any conflict of interest.

References

Amato T, Edzwald JK, Tobiason JE et al (2001) An integrated approach to dissolved air flotation. Water Sci Technol 43:19–26. https://doi.org/10.2166/wst.2001.0455

Amato T, Wicks J (2009) The practical application of computational fluid dynamics to dissolved air flotation, water treatment plant operation, design and development. J Water Supply Res Technol AQUA 58:65–73. https://doi.org/10.2166/aqua.2009.003

Azevedo A, Oliveira HA, Rubio J (2018) Treatment and water reuse of lead-zinc sulphide ore mill wastewaters by high rate dissolved air flotation. Miner Eng 127:114–121. https://doi.org/10.1016/j.mineng.2018.07.011

Bondelind M, Sasic S, Kostoglou M et al (2010a) Single- and two-phase numerical models of dissolved air flotation: comparison of 2D and 3D simulations. Coll Surf A Physicochem Eng Asp 365:137–144. https://doi.org/10.1016/j.colsurfa.2010.02.035

Bondelind M, Sasic S, Pettersson TJR et al (2010b) Setting up a numerical model of a DAF tank: turbulence, geometry, and bubble size. J Environ Eng 136:1424–1434. https://doi.org/10.1061/(ASCE)EE.1943-7870.0000275

Borhan A (1989) An experimental study of the effect of suspension concentration on the stability and efficiency of inclined settlers. Phys Fluids A 1:108–123. https://doi.org/10.1063/1.857539

Cagnetta C, Saerens B, Meerburg FA et al (2019) High-rate activated sludge systems combined with dissolved air flotation enable effective organics removal and recovery. Bioresour Technol 291:121833. https://doi.org/10.1016/j.biortech.2019.121833

Celik IB, Ghia U, Roache PJ et al (2008) Procedure for estimation and reporting of uncertainty due to discretization in CFD applications. J Fluids Eng Trans ASME 130:0780011–0780014. https://doi.org/10.1115/1.2960953

Crossley IA, Valade MT (2006) A review of the technological developments of dissolved air flotation. J Water Supply Res Technol AQUA 55:479–491. https://doi.org/10.2166/aqua.2006.057

Echeverri LF, Rein PW (2007) Numerical study of the flow in air flotation syrup clarifiers. Int Sugar J 109:372–378

Edzwald JK (2010a) Water quality & treatment: a handbook on drinking water. McGraw Hill, New York

Edzwald JK (2010b) Dissolved air flotation and me. Water Res 44:2077–2106. https://doi.org/10.1016/j.watres.2009.12.040

Emmanouil V, Skaperdas EP, Karapantsios TD, Matis KA (2007) Two-phase simulations of an off-nominally operating dissolved-air flotation tank. Int J Environ Pollut 30:213–230. https://doi.org/10.1504/IJEP.2007.014701

Emmanouil VA, Karapantsios TD, Matis KA (2011) Two- and three-phase simulations of an ill-functioning dissolved-air flotation tank. Int J Environ Waste Manag 8:215–228. https://doi.org/10.1504/IJEWM.2011.042632

Fang L, Jun M, Weichao M (2009) Removal of particles from water using dissolved air flotation. In: 3rd international conference on bioinformatics and biomedical engineering, iCBBE, pp 1–4. Doi: https://doi.org/10.1109/ICBBE.2009.5163313

Haarhoff J, Van Vuuren L (1993) A South African design guide for dissolved air flotation: report for the water research commission. Water research commission

Haarhoff J, van Vuuren LRJ (1995) Design parameters for dissolved air flotation in South Africa. Water Sci Technol 31:203–212. https://doi.org/10.1016/0273-1223(95)00218-C

Hedberg T, Dahlquist J, Karlsson D, Sörman LO (1998) Development of an air removal system for dissolved air flotation. Water Sci Technol 37:81–88. https://doi.org/10.1016/S0273-1223(98)00274-1

Hlukhov D, Larraona GS, Rivas A, Ramos JC (2022) Mono- and multi-diameter approaches to predict stratified flow structure by means of CFD simulations in DAF systems. J Water Process Eng 46:102624. https://doi.org/10.1016/j.jwpe.2022.102624

Ishii M, Mishima K (1984) Two-fluid model and hydrodynamic constitutive relations. Nucl Eng Des 82:107–126. https://doi.org/10.1016/0029-5493(84)90207-3

Jokela P, Lepistö R (2014) Lamella dissolved air flotation treatment of fish farming effluents as a part of an integrated farming and effluent treatment concept. Environ Technol 35:2727–2733. https://doi.org/10.1080/09593330.2014.919035

Kiuri HJ (2001) Development of dissolved air flotation technology from the first generation to the newest (third) one (DAF in turbulent flow conditions). Water Sci Technol 43:1–7. https://doi.org/10.2166/wst.2001.0450

Kwon SB, Park NS, Lee SJ et al (2006) Examining the effect of length/width ratio on the hydro-dynamic behaviour in a DAF system using CFD and ADV techniques. Water Sci Technol 53:141–149. https://doi.org/10.2166/wst.2006.218

Lakghomi B, Lawryshyn Y, Hofmann R (2015) A model of particle removal in a dissolved air flotation tank: importance of stratified flow and bubble size. Water Res 68:262–272. https://doi.org/10.1016/j.watres.2014.09.053

Lakghomi B, Lawryshyn Y, Hofmann R (2012) Importance of flow stratification and bubble aggregation in the separation zone of a dissolved air flotation tank. Water Res 46:4468–4476. https://doi.org/10.1016/j.watres.2012.05.038

Lundh M (2002) Effects of flow structure on particle separation in dissolved air flotation. Lund University, Water and environmental engineering. Lund, Sweden

Lundh M, Jönsson L (2005) Residence time distribution characterization of the flow structure in dissolved air flotation. J Environ Eng 131:93–102. https://doi.org/10.1061/(ASCE)0733-9372(2005)131:1(93)

Lundh M, Jönsson L, Dahlquist J (2001) The flow structure in the separation zone of a DAF pilot plant and the relation with bubble concentration. Water Sci Technol 43:185–194. https://doi.org/10.2166/wst.2001.0493

Lundh M, Jonsson L, Dahlquist J (2002) The influence of contact zone configuration on the flow structure in a dissolved air flotation pilot plant. Water Res 36:1585–1595. https://doi.org/10.1016/S0043-1354(01)00357-8

Lundh M, Jönsson L, Dahlquist J (2000) Experimental studies of the fluid dynamics in the separation zone in dissolved air flotation. Water Res 34:21–30. https://doi.org/10.1016/S0043-1354(99)00136-0

Manninen M, Taivassalo V, Kallio S (1996) On the mixture model for multiphase flow. VTT Publications, Spoo (Finland)

Moruzzi RB, Reali MAP (2014) The influence of floc size and hydraulic detention time on the performance of a dissolved air flotation (DAF) pilot unit in the light of a mathematical model. Bioprocess Biosyst Eng 37:2445–2452. https://doi.org/10.1007/s00449-014-1221-6

Piaggio AL, Soares LA, Balakrishnan M et al (2022) High suspended solids removal of Indian drain water with a down-scaled dissolved air flotation (DAF) for water recovery. Assessing water-type dependence on process control variables. Environ Chall 8:100567. https://doi.org/10.1016/j.envc.2022.100567

Reali MAP, Marchetto M (2001) High-rate dissolved air flotation for water treatment. Water Sci Technol 43:43–49. https://doi.org/10.2166/wst.2001.0461

Reyes C, Apaz F, Niño Y et al (2022) A review on steeply inclined settlers for water clarification. Miner Eng. https://doi.org/10.1016/j.mineng.2022.107639

Rodrigues JP, Béttega R (2018) Evaluation of multiphase CFD models for dissolved air flotation (DAF) process. Colloids Surf A Physicochem Eng Asp 539:116–123. https://doi.org/10.1016/j.colsurfa.2017.12.015

Satpathy K, Rehman U, Cools B et al (2020) CFD-based process optimization of a dissolved air flotation system for drinking water production. Water Sci Technol 81:1668–1681. https://doi.org/10.2166/wst.2020.028

Soares FA, Martins dos Santos B, Rosa SL et al (2021) Dissolved air flotation as potential new mechanism for intestinal parasite diagnosis in feces. Acta Trop 224:106137. https://doi.org/10.1016/j.actatropica.2021.106137

Ta CT, Beckley J, Eades A (2001) A multiphase CFD model of DAF process. Water Sci Technol 43:153–157. https://doi.org/10.2166/wst.2001.0488